Explicit Model-Predictive Control of a PWM Inverter With an *LCL* Filter

Sébastien Mariéthoz, *Member, IEEE*, and Manfred Morari, *Fellow, IEEE*

***Abstract*—This paper deals with the control of pulsewidth modulation inverters connected to the grid through resonant *LCL* filters. It proposes two alternative (piecewise affine) models that account for the switched behavior of the converter. Based on these improved models, an explicit model-predictive control scheme is derived in order to provide a fast response, making it very suitable for applications, such as active filtering, where a large bandwidth is required. A state observer and a grid voltage estimator are used in order to reduce the number of required sensors and to eliminate noise. The control scheme relies only on filtered current measurements and on the dc voltage.**

***Index Terms*—Active damping, explicit model-predictive control (EMPC), Kalman filter, *LCL* filter, pulsewidth-modulation (PWM) inverter.**

I. Introduction

As THE requirements for improved power quality and reduced converter size and weight are increasing, high-order filters are becoming a more attractive solution to connect a converter to the grid [1]. However, the design and stabilization of these resonant filters require some care, and the synthesis of an effective controller is a challenging task, particularly when a large bandwidth is required. The analysis of some classical methods have shown that they cannot achieve stability in some cases [2], [3].

The purely passive stabilization solution consists in introducing a damping resistor, generally in parallel to the grid inductor [4]. This diminishes the oscillator quality factor, which helps in stabilizing the filter; at the same time, however, it reduces its filtering and energy efficiencies. In order to avoid this efficiency reduction, many solutions have been proposed to replace the dissipative damping solution by control schemes that feature active damping [5]–[10]. Among these, the most intuitive simply mimics the effect of a damping resistor by appropriately acting on the inverter voltage.

Some important issues related to the control of these converters have been partially tackled in different research works.

The robustness of the controller against grid disturbances is investigated in [11]. A close inspection of the control problem reveals that the capability of the controller to reject grid disturbance mostly depends on the accuracy of the grid voltage measurement. On the other hand, considering the large number of state variables and disturbances in the system, it is desirable to reduce the number of required sensors, which makes more difficult the estimation of the system variables. Different solutions have been proposed, based on various estimation schemes. A voltage sensorless scheme that requires a minimum number of transducers is proposed in [10].

Once the stability of the resonant filter is obtained, another crucial issue for applications, such as active filtering, is the fast tracking of the compensation current, which directly affects the grid THD [12]. In this context, optimal control offers an important potential to guarantee stability and *also improve the dynamic performance*, particularly in difficult operating conditions. Linear quadratic regulation (LQR) provides stability and performance. Its weaknesses stem from the difficulty to account for system constraints and from the absence of systematic approach to tune the penalty matrices to obtain the desired performance. A modification of the LQR scheme is proposed in [13] to limit the inverter currents.

In model-predictive control (MPC), the constraints are included at the controller design stage as linear inequalities in the optimal control problem, avoiding any afterward modification of the control scheme, which could jeopardize its performance or stability. The limitations on the control variables (the inverter duty cycles) are also included in the same way, which reduces the tuning effort of the penalty matrices in the optimization problem. Additional parameters, such as known disturbances, are also included in the optimization to obtain an accurate reference tracking.

In the past, MPC has only been applied to slow systems (e.g., chemical plants) due to the large numbers of complex computations that were required to solve the optimization problem at each sampling instant. The growth of the computational power available and some recent research works have shown the potential of the technique in power electronics applications. Two different techniques must be distinguished.

A. Finite-State Predictive Control

All possible switch combinations are considered and evaluated at each sampling instant [14]. An attractive aspect of this approach is that any expression that can be evaluated with a microprocessor can be used as model and cost function. The major drawback is the difficulty to limit the switching frequency. A solution to minimize the switching frequency with a similar approach has been proposed in [15] and [16].

B. MPC

The control variable is generally a duty cycle or space vector that varies continuously between its minimum and maximum

Manuscript received July 22, 2008; revised October 13, 2008. First published November 7, 2008; current version published January 30, 2009.

The authors are with the Automatic Control Laboratory, Swiss Federal Institute of Technology, 8092 Zürich, Switzerland (e-mail: mariethoz@control.ee.ethz.ch).

Digital Object Identifier 10.1109/TIE.2008.2008793

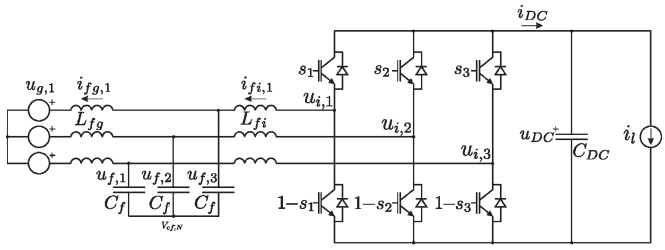

Fig. 1. Active front-end voltage-source inverter and its filter.

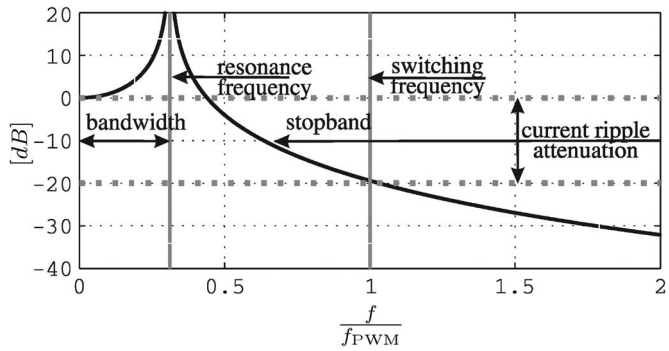

Fig. 2. *LC* filter frequency response. The filter is characterized by the ratio resonance over switching frequency, which determines the bandwidth and attenuation at the switching frequency.

value. The drawback is that the model must generally be linear or piecewise affine (PWA) and the cost function must be quadratic or use one or infinite norms. Dynamic programming is generally used to solve the associated constrained finite-time optimal control problem. This paper deals with this technique.

In both cases, a discrete-time model is necessary. The most common model used for the control synthesis is the classical zero-order hold model. The main feature of this model is to neglect the switching and to only capture the converter average behavior. This is, most of the time, sufficient and desirable as this can easily be used with classical controller synthesis tools. The effect of the switching can, however, be taken into account using a hybrid model in MPC [17]. This is interesting in some cases, as a significant discrepancy between the average model prediction and the actual sampled state evolution can appear and provoke a significant variation of the closed-loop system behavior when the filter resonance and switching frequencies are very close [3].

This paper describes a discrete model of the inverter that accounts precisely for the applied voltage pattern for two types of pulsewidth-modulation (PWM) techniques. An MPC scheme that allows stable converter operation and effective current tracking is derived based on that model. Constraints, such as maximum admissible current and duty-cycle saturation, are directly taken into account at the controller design stage and inherently satisfied by the controller algorithm. The control scheme is extended with a state observer and a grid voltage estimator, which allow for limiting the number of required sensors. The scheme relies only on the three filtered currents and the dc voltage measurements. Finally, simulation and experimental results are presented for the application of the proposed control scheme to active power filtering.

II. Discrete-Time Model Derivation

In this section, the system is analyzed, and the discrete-time control model that is necessary for the synthesis of the model-predictive controller is derived.

The converter system is shown in Fig. 1. A two-level three-phase converter connects an ac grid to a dc load. An *LCL* filter removes the current ripple. The filter damping and bandwidth are mainly characterized by the ratio resonance over switching frequencies. The *LC* filter (that is added to the *L* boost inductor to form the *LCL* filter) frequency response is shown in Fig. 2. The bandwidth increases with the resonance frequency while, at the same time, the damping factor and filter weight diminish; hence, a tradeoff has to be found.

The grid impedance which is not part of the converter is not represented here; however, it can be accounted for in L_{fg}. A common mode filter is sometimes added but it is not considered here, as it does not directly affect the control.

A. System Continuous-Time Dynamics

By neglecting the *LCL* filter losses and the nonlinear behavior of the circuit components (mainly pronounced for the coils), the dynamic behavior of the overall three-phase converter system shown in Fig. 1 is described by the following equations:

$$\frac{d\underline{\boldsymbol{x}}(t)}{dt} = \boldsymbol{A}_c\left(\underline{\boldsymbol{s}}(t)\right)\underline{\boldsymbol{x}}(t) + \boldsymbol{C}_c\underline{\boldsymbol{u}}_g(t) + \boldsymbol{D}_c i_l(t) \qquad (1)$$

with

$$\boldsymbol{A}_c = \begin{bmatrix} 0 & 0 & -\frac{1}{L_{fi}} & \frac{\underline{s}(t)}{L_{fi}} \\ 0 & 0 & -\frac{1}{L_{fg}} & 0 \\ \frac{1}{C_f} & -\frac{1}{C_f} & 0 & 0 \\ -\frac{\underline{s}^*(t)}{C_{\mathrm{DC}}} & 0 & 0 & 0 \end{bmatrix}$$

$$\boldsymbol{C}_c = \begin{bmatrix} 0 \\ -\frac{1}{L_{fg}} \\ 0 \\ 0 \end{bmatrix}$$

$$\boldsymbol{D}_c = \begin{bmatrix} 0 \\ 0 \\ 0 \\ -\frac{1}{C_{\mathrm{DC}}} \end{bmatrix}$$

$$\underline{\boldsymbol{x}}(t) = \begin{bmatrix} \underline{i}_{fi} \\ \underline{i}_{fg} \\ \underline{u}_f \\ u_{\mathrm{DC}} \end{bmatrix}.$$

In these equations, $\underline{\boldsymbol{u}}_g(t)$, $\underline{\boldsymbol{i}}_{fi}(t)$, $\underline{\boldsymbol{i}}_{fg}(t)$, and $\underline{\boldsymbol{u}}_f(t)$ are space vectors in a complex number notation, such that $\underline{\boldsymbol{i}}_{fg}(t) = i_{fi,\alpha}(t) + j i_{fi,\beta}(t)$; $\underline{\boldsymbol{s}}(t)$ is the "instantaneous" switch space vector, and $\underline{\boldsymbol{s}}^*(t)$ is its complex conjugate; $\underline{\boldsymbol{u}}_g(t)$ is the grid voltage applied to the filter output; $\underline{\boldsymbol{i}}_{fi}$ is the current injected into the filter; $\underline{\boldsymbol{i}}_{fg}(t)$ is the filtered current injected into the grid; $\underline{\boldsymbol{u}}_f(t)$ is the filtering capacitor voltage; u_{DC} is the dc-link voltage; i_l is the dc-load current; L_{fi} is the inductance of the filtering inductor connected to the inverter; L_{fg} is the

inductance of the filtering inductor connected to the grid; C_f is the capacitance of the filtering capacitor; and C_{DC} is the dc-link capacitor.

Although the *LCL* filter subsystem is linear, the overall converter system (1) is nonlinear as the switching changes the circuit topology by connecting the dc capacitor terminals to the ac phases. Moreover, in the absence of neutral connection, the phases are coupled.

B. Classical Discrete Control Model

In many applications, the dc-link capacitor is relatively large, and its dynamics is slow compared with the filter dynamics; hence, the state variable u_{DC} in (1) can be replaced by a time-varying parameter, yielding a linear continuous-time system model of the form

$$\frac{d\underline{\boldsymbol{x}}(t)}{dt} = \boldsymbol{A}_f \underline{\boldsymbol{x}}(t) + \boldsymbol{B}_f \underline{\boldsymbol{u}}_i(t) + \boldsymbol{C}_f \underline{\boldsymbol{u}}_g(t) \tag{2}$$

with $\underline{\boldsymbol{u}}_i(t) = \underline{\boldsymbol{s}}(t) \cdot u_{\mathrm{DC}}(t)$ [matrices are defined by (23)]. Due to the switching, the discrete equivalent of that continuous-time linear model is, however, still nonlinear. This nonlinearity is usually neglected as the PWM voltage pattern is approximated by a zero-order hold equivalent. The PWM voltage pattern shown in Fig. 3(a) is therefore approximated by its average equivalent shown in Fig. 3(b). A discrete-time linear model can thus be obtained using this approximation

$$\boldsymbol{x}_{k+1} = \boldsymbol{A} \cdot \boldsymbol{x}_k + \boldsymbol{B}_0 \cdot \underbrace{d_k}_{\text{duty cycle}} \cdot u_{\mathrm{DC},k} + \boldsymbol{C}_0 \cdot \underbrace{u_{g,k}}_{\text{grid voltage}} \tag{3}$$

where only a single-phase system is considered for simplicity. k is the sampling instant index; $\boldsymbol{A} = e^{\boldsymbol{A}_f \cdot T_s}$ is the exact evolution of the state variables obtained using the matrix exponential; $\boldsymbol{B}_0 = \int_0^{T_s} e^{\boldsymbol{A}_f \cdot \tau} \cdot d\tau \cdot \boldsymbol{B}_f$ and $\boldsymbol{C}_0 = \int_0^{T_s} e^{\boldsymbol{A}_f \cdot \tau} \cdot d\tau \cdot \boldsymbol{C}_f$ are obtained using a zero-order hold approximation of the effect of the duty cycle and grid voltage on the system.

This representation is very often sufficient to synthesize a controller. It is, however, well known that some stability issues occur in converter systems with resonant filters, partly due to the switching. Indeed, as the PWM modulation is nonlinear, the zero-order hold model gives an exact representation of the modulation only when the duty-cycle value is zero or one.

C. Discrete-Time Model With Symmetrical PWM Approximation

An "exact" representation of the evolution of the discrete system state over one sampling period can be derived for each duty cycle

$$\boldsymbol{x}_{k+1} = \boldsymbol{A} \cdot \boldsymbol{x}_k + \boldsymbol{B}(d_k) \cdot d_k + \boldsymbol{C}_0 \cdot u_{g,k}. \tag{4}$$

$\boldsymbol{B}(d_k)$ depends on the chosen duty cycle (the factor $u_{\mathrm{DC},k}$ is omitted for simplicity). This expression can be used to obtain a better evaluation of $\boldsymbol{x}_{k+1}$ when the duty cycle is in the vicinity of the selected duty cycle D_0

$$\boldsymbol{x}_{k+1} = \boldsymbol{A} \cdot \boldsymbol{x}_k + \boldsymbol{X}_0 + \boldsymbol{B}_p \cdot (d_k - D_0) + \boldsymbol{C}_0 \cdot u_{g,k} \tag{5}$$

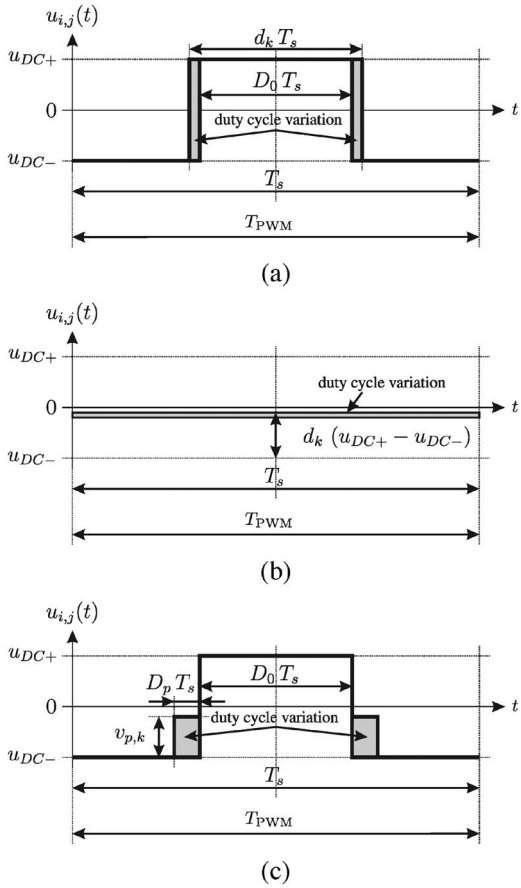

Fig. 3. Symmetrical triangular carrier modulation. PWM voltage pattern and its investigated control models. (a) Symmetrical PWM. (b) Zero-order hold linear approximation. (c) PWA approximation.

where the vector $\boldsymbol{X}_0 = \boldsymbol{B}(D_0) \cdot D_0$ characterizes the evolution of the state due to the duty cycle D_0 and where the matrix $\boldsymbol{B}_p$ characterizes the variation of this evolution for a small variation of the duty cycle. A linear characterization $\boldsymbol{B}_p$ can be obtained by applying two pulses of constant width $D_p T_s$ with a height $v_{p,k}$ proportional to the variation of the duty cycle around the edges of the base pulse corresponding to D_0, as shown in Fig. 3(c). The pulse height is found by imposing that the voltage pattern surfaces are the same in Fig. 3(a) and (c); hence,

$$v_{p,k} = \frac{d_k - D_0}{D_p} \cdot (u_{\mathrm{DC}+} - u_{\mathrm{DC}-}). \tag{6}$$

The analytical derivation of matrices $\boldsymbol{A}$, $\boldsymbol{B}_p$, and $\boldsymbol{X}_0$, which characterizes the improved model, is shown in Appendix B.

A duty-cycle variation will affect the voltage pattern at the same place for the real voltage pattern and its approximation. The smaller the D_p, the more accurate the approximation; however, the smaller the domain of validity, $d_k \in [D_0, D_0 + 2D_p]$ of the approximation. It is necessary to use several of these approximations to cover the full possible range of duty cycles

$$\begin{aligned} \boldsymbol{x}_{k+1} &= \boldsymbol{A} \cdot \boldsymbol{x}_k + \boldsymbol{B}_{p,j} \cdot d_k + \boldsymbol{X}_{0,j} + \boldsymbol{C}_0 \cdot u_{g,k} \\ d_k &\in [D_j, D_j + 2D_p] \\ j &\in \left\{1, 2, \ldots, \frac{1}{2D_p}\right\}. \end{aligned} \tag{7}$$

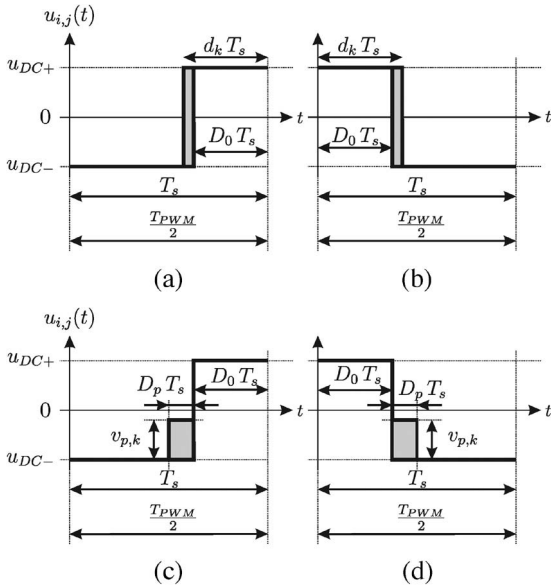

Fig. 4. Asymmetrical triangular carrier modulation. PWM voltage pattern and proposed control model; the binary variable m allows one to select alternately the left and right patterns. (a) Low to high transition. (b) High to low transition. (c) Approximation k even, $m = 0$. (d) Approximation k odd, $m = 1$.

Each subsystem is affine; the overall system is hybrid PWA. By construction, continuity is imposed between the affine models at the boundaries

$$\boldsymbol{B}_j \cdot D_j + \boldsymbol{X}_j = \boldsymbol{B}_{j+1} \cdot D_j + \boldsymbol{X}_{j+1} \quad \forall j \in \left\{1, 2, \ldots, \frac{1}{2D_p} - 1\right\}. \quad (8)$$

In (7), the same pulsewidth D_p has been taken for all intervals. In some cases, it is however advised to take intervals of varying widths to reduce complexity and obtain enough accuracy where required.

D. Discrete-Time Model With Asymmetrical PWM Approximation

When the computation time available allows for a sampling frequency higher than the switching frequency, the bandwidth can be increased (roughly doubled) by using asymmetrical (triangular carrier) PWM. As two transitions can be adjusted on this voltage pattern, the duty cycle is changed twice per modulation period. The sampling period is then halved, which allows for a faster response time and the tracking of faster references.

The main characteristics of this modulation is that a voltage pattern with a transition from low to high-level alternates with a voltage pattern with a transition from high to low level, as shown in Fig. 4(c) and (d). A binary state variable is required to characterize the voltage pattern alternance

$$m_k = 1 - m_{k-1}. \quad (9)$$

Based on m, the voltage pattern of either Fig. 4(c) or (d) is selected. The model derivation is similar to the model derivation with symmetrical PWM.

E. System Model for Three-Phase Systems and Space Vector PWM

The voltage pattern for three-phase systems is the same, even if space vector modulation is used. For three-phase systems without neutral wire connection, the common mode voltage has no effect on the system; the corresponding duty cycles, however, affect the ripple waveform, and this reduces the single-phase model accuracy when used in this situation.

III. Control Strategy

A. MPC

In MPC, the control objectives are formulated as a cost function to minimize over a prediction horizon while respecting the system constraints. The evolution of the state over the prediction horizon is evaluated by using the discrete-time control model obtained in Section II, which enters the optimization problem as a set of equality constraints.

1) Cost Function: The cost function reflects the objective, which is to minimize the tracking error

$$\min_{d_k \ldots d_{k+N-1}} J(\boldsymbol{x}_{c,k}) = \sum_{n=1}^{N} Q_n \cdot \|i_{\text{ref},k} - i_{fg,k+n}\|_1 + R_n \cdot \|u_{g,k} - d_{k+n-1}\|_1. \quad (10)$$

The controller state $\boldsymbol{x}_{\text{c},k}$ is a parameter for the optimization, which comprises the initial plant state $\boldsymbol{x}_k$, the reference $i_{\text{ref},k}$, and the estimated grid voltage $u_{g,k}$, while the optimal sequence of duty cycles $d_k, d_{k+1}, \ldots, d_{k+N-1}$ and corresponding sequence of predicted states $\boldsymbol{x}_{k+n}$ are the sought results of the optimization.

The variables have been scaled by the dc voltage $u_{\text{dc},k}$ in order to obtain a system model that depends only on the duty cycle and not on the dc voltage. This allows one to obtain fixed boundaries in the control problem as the affine dynamics is selected based on the duty-cycle value. A second term is added to the cost function to limit the difference between the inverter ac voltage and the utility grid voltage. The utility of this term will be discussed in Section III-A3.

2) Prediction Model, Equality Constraint: The evolution of the state is predicted over a finite horizon using the control model (7)

$$\begin{aligned} \boldsymbol{x}_{k+n} &= \boldsymbol{A} \cdot \boldsymbol{x}_{k+n-1} + \boldsymbol{B}_{p,j} \cdot d_{k+n-1} + \boldsymbol{X}_{0,j} + \boldsymbol{C}_0 \cdot u_{g,k} \\ d_k &\in [D_j, D_j + 2D_p] \\ j &\in \left\{1, 2, \ldots, \frac{1}{2D_p}\right\} \\ D_1 &= D_{\min} \\ D_{\frac{1}{2D_p}+1} &= D_{\max}. \end{aligned} \quad (11)$$

As the reference is quickly changing, the prediction horizon can be selected to be relatively short; it, however, has to be long enough to capture the resonant filter behavior (at least two or three sampling times in our case).

3) Inequality Constraints: The duty cycle has to be bounded to account for the converter limitation and prevent impossible control sequences to be selected

$$D_{\min} \leq d_{k+n} \leq D_{\max}. \tag{12}$$

This inequality constraint limits the duty cycle and makes the second term of the cost function (proportional to R_n) optional. This is one of the main differences between linear quadratic optimal control and MPC. In the first, both the tracking error and the duty cycle must be weighted. The weight must somewhat be tuned to reflect the duty-cycle limitations and to reach the desired performance. In MPC, the weight on the actuator control input is replaced by boundary constraints that reflect the real actuator capability, which considerably reduces the tuning effort. The weight on the actuator control input is, however, kept, as it allows for the reduction of the converter sensitivity to the measurement noise when necessary.

4) Cost Function Based on the Envelope: The main consequence of the ripple is the deterioration of the quality of the tracking or even destabilization of the system when fed back to classical controllers. The PWA control model predicts this ripple, which is therefore no longer seen as a disturbance to compensate, thus avoiding instability. The cost function (10) features the error between the predicted discrete-time signal which contains a small ripple and its reference which does not contain any ripple. However, the goal here is to minimize the error on the signal envelope while this cost function minimizes the error on the signal envelope lifted by the actual ripple, which slightly increases the tracking error.

The performance can be slightly improved by predicting the intermediate values of the state between two sampling instants and by subtracting these values to the reference. The error signal obtained, which gives a better approximation of the error on the current envelope, is penalized in the cost function. It has to be noted that this approach does not change the controller structure and that no additional measurement or control action is taken in that case (differently from what is done with multiple sampling [18]).

B. EMPC

The optimal control problem is completely characterized by the cost function (10), the equality constraints (11), and the inequality constraints (12). In explicit MPC (EMPC), this discrete-time optimal control problem is reformulated as a multiparametric program, as described in [19] and [20]. This program is solved offline for all possible states, resulting in a lookup table giving the optimal solution as a function of the control state $\boldsymbol{x}_{\mathrm{c},k}$, which allows for a very fast execution of the control algorithm.

As the model is PWA and as the constraints are linear inequalities, the solution is PWA, and the state space is consequently partitioned into several polyhedral regions. In each region, the optimal solution is an affine function of the controller state $\boldsymbol{x}_{\mathrm{c},k}$. For the considered application, assuming that the state lies in region r, the optimal duty cycle d_k at instant k is obtained through a function of the form

$$d_k = \boldsymbol{k}_r \cdot \boldsymbol{x}_{c,k} + c_r \tag{13}$$

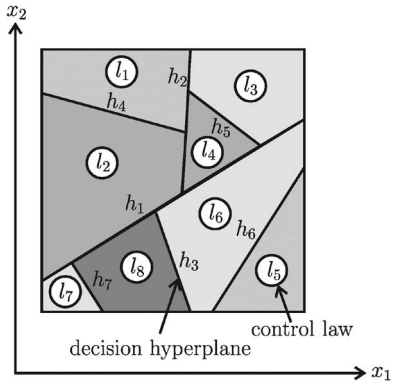

Fig. 5. State space is divided into eight regions delimited by seven hyperplanes (lines in 2-D) $h_i, i \in \{1 \dots 7\}$. Each region is associated to a control law $l_p, p \in \{1 \dots 8\}$. Example shown here is in 2-D; the proposed controller is 5-D.

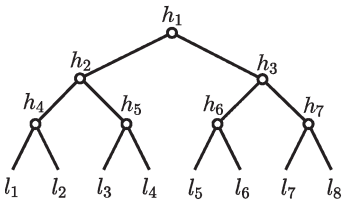

Fig. 6. Binary search tree example, with seven nodes corresponding to the decision hyperplanes $h_i, i \in \{1 \dots 7\}$ leading to eight control laws $l_p := \{\boldsymbol{k}_p, c_p\}$, $p \in \{1 \dots 8\}$. The depth of shown tree is three; the proposed controller tree depth is eight.

where $\boldsymbol{k}_r$ is the feedback gain in region r and c_r is a constant term. The region to which the controller state $\boldsymbol{x}_{\mathrm{c},k}$ belongs can be determined in two ways.

1) Direct Region Membership Determination: Each region p is defined by a set of hyperplanes $\{h_j, j \in H_p\}$, where H_p denotes the index set of hyperplanes delimiting the considered polyhedron. One has to evaluate on which side of the boundary the state is to determine if the state belongs to a given polyhedral region p. Thus, membership to a region is established by checking the condition

$$\boldsymbol{x}_{c,k} \in \text{region } p \text{ if } f_j \boldsymbol{x}_{c,k} \geq 0 \qquad \forall j \in H_p \tag{14a}$$

$$f_j \boldsymbol{x}_{c,k} = \boldsymbol{a}j \cdot \boldsymbol{x}_{c,k} + b_j. \tag{14b}$$

The implementation requires the evaluation of (14b) for all hyperplanes delimiting a region, and this procedure has to be repeated for each region. Once the region r containing the state is found, the search process can be interrupted, and the optimal duty cycle is obtained using (13).

2) EMPC Implementation With Binary Search Tree: As the hyperplanes divide the state space into regions, a more efficient implementation of the membership test (14a) and (14b) can be obtained using a binary search tree, thus avoiding the evaluation for several times of the same hyperplane. At each node, the sign of an affine function of the form (14b) is evaluated to select the next branch. At the last leaf, the optimal solution is obtained by computing (13). The biggest difficulty, then, actually consists in building the binary search tree offline. Fig. 6 shows the binary search tree associated to Fig. 5. In the shown example, the optimal control input is obtained after computing four affine functions and three sign evaluations.

C. State Observer

In [10], the measured current is represented by the inverter currents (i_{fi}); then, considering only low-frequency components and based on instantaneous power theory, the capacitor and grid voltages are estimated. Here, separate observer and estimator are used for the full state and grid voltage estimations. It can be cheaper to measure the inverter current when the sensor is integrated in the converter module or when the currents are measured with shunts placed in series with the leg bottom switches. On the other hand, the objective is to control the filtered currents; therefore, better results can be obtained with respect to model mismatches by directly measuring these currents. Moreover, the requirements on the transducer are reduced, and the noise immunity is increased if the filtered currents are measured. Hence, in this paper, the measured variables are the filtered currents and the dc-link voltage. As the inverter currents and the capacitor voltages are required for the control scheme, a model-based state observer is used to construct an estimation of the state. The same model is used for the explicit model-predictive controller synthesis and for the observer which has the structure of a Kalman filter

$$\begin{aligned}\hat{\boldsymbol{x}}_{k+1} &= \boldsymbol{A}\hat{\boldsymbol{x}}_k + \boldsymbol{B}_{p,j}(d_k - D_j)u_{\mathrm{DC},k} \\ &\quad + \boldsymbol{X}_{0,j} + \boldsymbol{C}_0\hat{u}_{g,k} + \boldsymbol{L}_j(i_{fg,k} - \hat{i}_{fg,k}) \\ d_k &\in [D_j, D_j + 2D_p]. \end{aligned} \tag{15}$$

The computation delay is also compensated through this observer. The feedback matrix $\boldsymbol{L}_j$ is obtained numerically using a Matlab Kalman filter function.

D. Grid Voltage Estimator

The performance of the inverter is conditioned by the quality of the grid voltage estimation, which is required to reconstruct the state with the observer (15). The grid voltage estimation is also required to synchronize the converter with the grid in order to generate active or reactive power or to synchronize the active filtering algorithm. The proposed grid-voltage-estimation scheme is based on the comparison of the actual inverter current and its estimated evolution using the grid voltage estimation. The measured error between these two values is used to correct the grid voltage estimation.

The measured error between the prediction $\hat{i}_{fg,k}$ and the measured value of the current $i_{fg,k}$ is due to the modeling errors, the noise, and the error between the actual grid voltage and its estimated value

$$\epsilon_{g,k} = u_{g,k} - \hat{u}_{g,k}. \tag{16}$$

If we assume the modeling errors and noise to be negligible (it can be filtered later), then we have

$$\begin{aligned}\hat{i}_{fg,k} &= \boldsymbol{A}_1\hat{\boldsymbol{x}}_{k-1} + \boldsymbol{B}_{p,j,1}(d_{k-1} - D_j)u_{\mathrm{DC},k} \\ &\quad + \boldsymbol{X}_{0,j,1} + \boldsymbol{C}_{0,1}\hat{u}_{g,k-1}, \qquad d_k \in [D_j, D_j + 2D_p] \end{aligned} \tag{17a}$$

$$\begin{aligned}i_{fg,k} &= \boldsymbol{A}_1\hat{\boldsymbol{x}}_{k-1} + \boldsymbol{B}_{p,j,1}(d_{k-1} - D_j)u_{\mathrm{DC},k} \\ &\quad + \boldsymbol{X}_{0,j,1} + \boldsymbol{C}_{0,1}u_{g,k-1}, \qquad d_k \in [D_j, D_j + 2D_p] \end{aligned} \tag{17b}$$

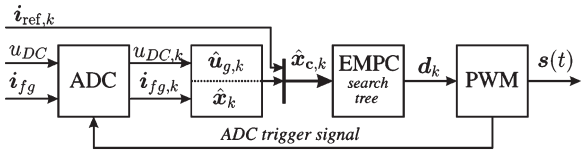

Fig. 7. Control algorithm block diagram.

where index 1 on the matrices indicate that only the first line is taken. By subtracting (17a) from (17b), we obtain

$$i_{fg,k} - \hat{i}_{fg,k} = \boldsymbol{C}_{0,1}(u_{g,k-1} - \hat{u}_{g,k-1}). \tag{18}$$

$\epsilon_{g,k}$ is then obtained as

$$\epsilon_{g,k} = \frac{i_{fg,k} - \hat{i}_{fg,k}}{\boldsymbol{C}_{0,1}}. \tag{19}$$

The new grid voltage estimation can then be built by summing the correction to the previous estimation

$$\hat{u}_{g,k} = \hat{u}_{g,k-1} + \epsilon_{g,k}. \tag{20}$$

As $\epsilon_{g,k}$ also carries the current measurement noise, it is necessary to filter the grid voltage thus obtained and to compensate the phase shift introduced by the filtering.

E. Overall Current Controller Implementation

The complete control algorithm is shown in Fig. 7. The analog-to-digital converters are triggered by the PWM generator. The measured variables are fed into the state observer and grid voltage estimator. The estimated state, estimated grid voltage, and current reference are fed as optimization parameters to the EMPC. The EMPC block features the binary search tree algorithm of Section III-B2 shown in Fig. 6. The thus-obtained duty cycles are applied to the PWM generator for the next period.

IV. Simulation Results

A. System Description

The proposed current-control scheme has been validated by simulation on an active power filter system. The open-loop frequency algorithm presented in [21] is used to predict the harmonic load that serves as reference to the current controller. There is a delay of one sampling period between the sampling and the application of the new duty cycle.

The explicit model-predictive controller is synthesized using the proposed PWA model with four duty-cycle intervals to predict the discrete-time state evolution. The prediction horizon N is three; the weights for the cost function (10) are $Q_n = 100$ and $R_n = 1$. The number of duty-cycle intervals and the horizon length are kept short as the complexity of the optimization and the size of the resulting search tree directly grow with them. Moreover, a bigger number of duty-cycle intervals or longer horizons do not practically bring any significant advantage for this application. The weights do not affect the controller

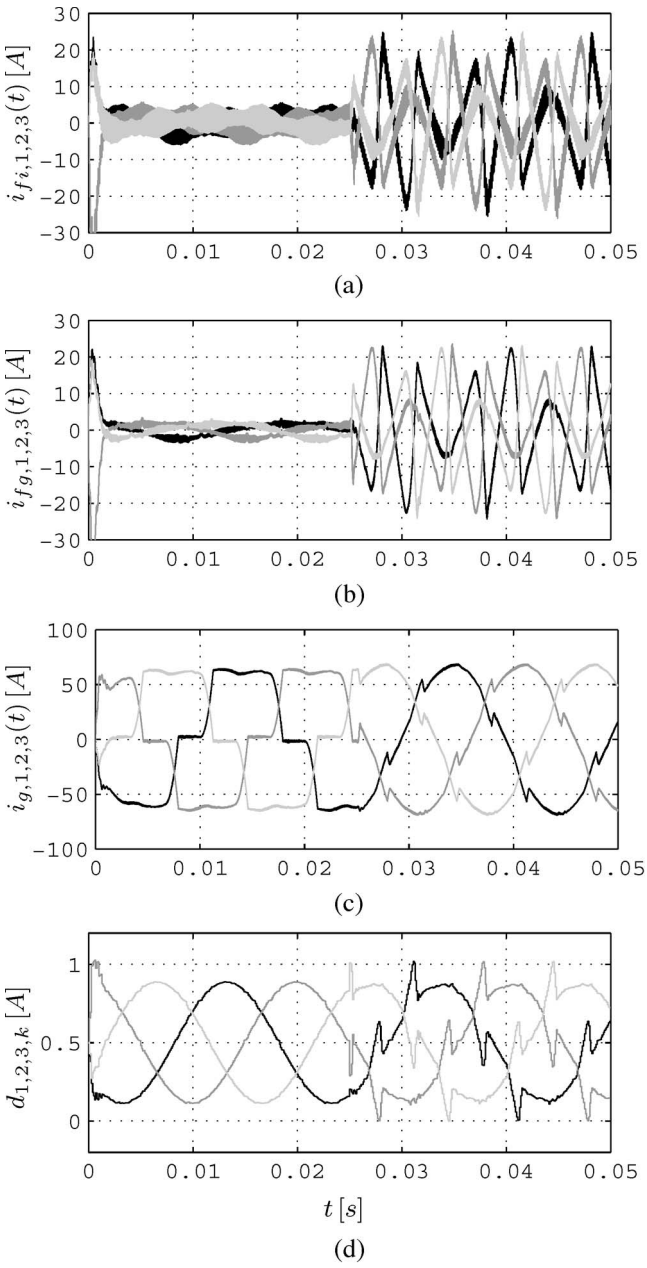

Fig. 8. Simulation plot: operation as pure active filter. (a) Inverter currents. (b) Active filter currents. (c) Grid currents. (d) Duty cycles.

performance much, as the duty cycle is already constrained by the optimization; however, a nonzero $R_n = 1$ allows one to reduce sensitivity to the noise and model mismatches.

B. Current Tracking

Some selected results are shown in Fig. 8. The nonlinear load to be compensated is a current-mode diode rectifier which draws 120° square current pulses from the grid, as shown between $t = 0$ s and $t = 0.025$ s in Fig. 8(c). The diode rectifier and the inverter are switched on at time zero, and the harmonic compensation is activated at $t = 0.025$ s. Fig. 8(d) features the duty cycles. It can be verified that no oscillation follows the abrupt transitions of the current reference. The grid current is properly filtered except those close to the diode rectifier transitions, where a distortion remains due to the current controller and PWM delays. A zoomed view of the tracking error is shown in Fig. 9. The filtered current follows the reference with a delay of approximately two sampling periods, which correspond to the computation time and to the PWM response; the tracking of the controller is nearly ideal. This delay cannot be eliminated; its effect on the compensation can, however, be eliminated at steady state by adjusting the reference appropriately, for instance, using the closed-loop frequency algorithm described in [21].

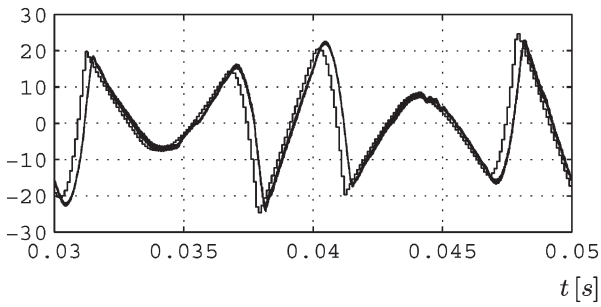

Fig. 9. Simulation plot. Zoom on the reference and current for one phase; the injected current follows the reference with a delay of approximately two sampling periods.

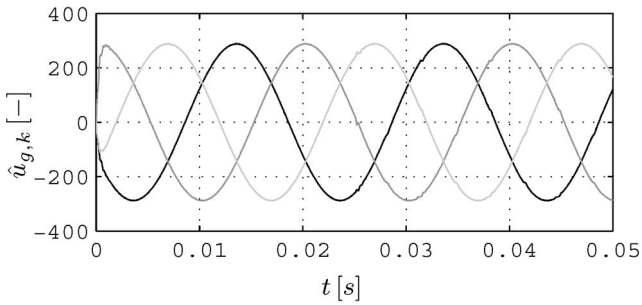

Fig. 10. Simulation plot. Estimated grid voltage.

C. Grid Voltage Estimation

The grid voltage estimation is shown in Fig. 10. It can be seen that it is a little bit distorted when the filtered current presents an abrupt transient; this is due to modeling errors. The voltage signal is filtered to eliminate the noise *inherently* captured by the estimator. The filter has a zero phase lag at grid frequency. The dynamics of the filter must be selected carefully to avoid deteriorating the overall system stability and performance.

The high current rise at startup [nearly equal to the nominal converter current, shown in Fig. 8(a) and (b)] is due to the convergence time of the voltage estimation. This could be removed by starting the estimation during the dc-link precharge (which is not simulated here).

V. Experimental Results

A prototype rated at 6 kV · A, 10 kHz, and 230 V has been built and used to validate the proposed control strategy.

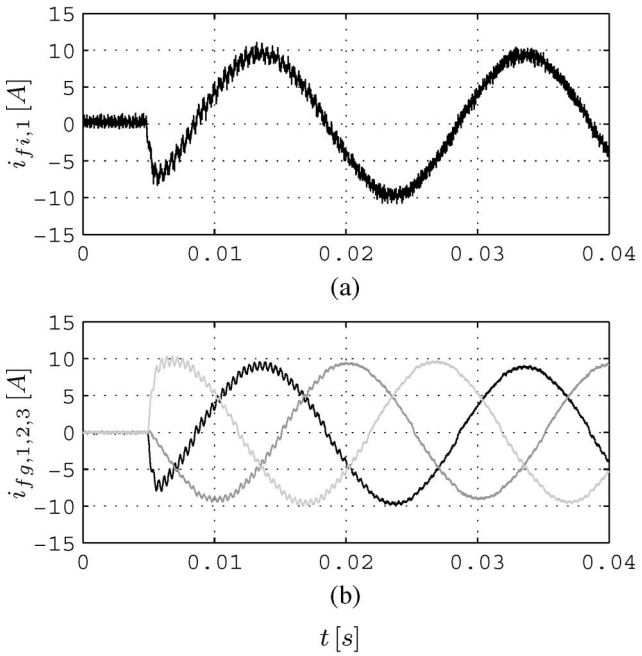

Fig. 11. Experimental plots. MPC with classical linear model; the inverter operates as a three-phase active front-end injecting three balanced sine currents onto the utility grid. Ten-kilohertz switching. Twenty-kilohertz sampling. Asymmetrical triangular PWM modulation. Fifty-hertz grid. (a) Inverter current. (b) Filtered currents t (in seconds).

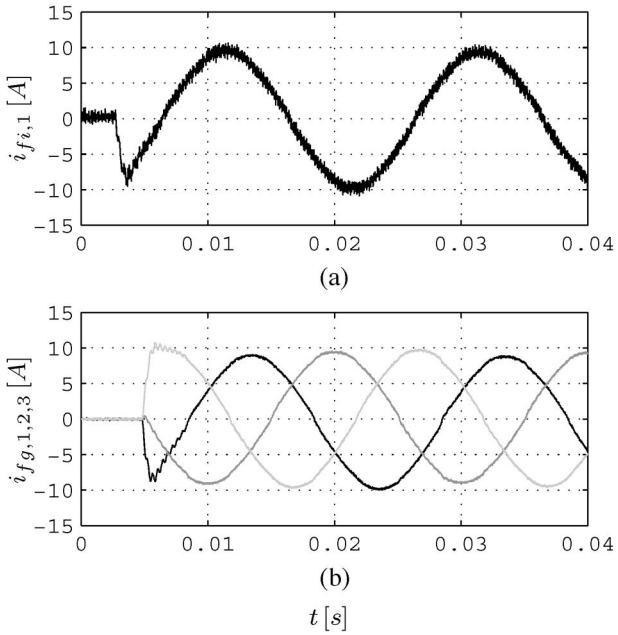

Fig. 12. Experimental plots. MPC with proposed PWA model; the three-phase IGBT inverter operates as a three-phase active front-end injecting three balanced sine currents onto the utility grid. Ten-kilohertz switching and sampling. Symmetrical triangular PWM modulation. Fifty-hertz grid. (a) Inverter current. (b) Filtered currents t (in seconds).

The control algorithms are implemented in C using integer arithmetic on a 16-b fixed-point Analog Device Blackfin DSP.

The optimal control problem is formulated and solved using Yalmip [22] and MPT [23] toolboxes in Matlab. The binary search tree is also built using MPT and subsequently transformed into a set of C code arrays that are used by the EPMC algorithm.

With four intervals of the duty cycle (four affine approximations over four even intervals of the duty cycle), the considered controller (for which the results are presented in the next sections) has 124 regions with 23 different control laws, and the depth of the binary search tree is eight. A maximum of eight iterations is thus required to obtain the optimal duty cycle. The time to run the overall algorithm shown in Fig. 7 is 20 μs.

Some selected results are presented in the following sections (circuit parameters can be found in Appendix C).

A. Operation as Sine Active Front End

1) MPC Based on Classical Average Model: As shown in Fig. 11, a model-predictive controller is tested using asymmetrical triangular PWM to generate the voltage pattern and using an average model (that does not capture the effect of switching) to synthesize the controller. The current controller reference is set to zero until $t = 5$ ms. At $t = 5$ ms, a three-phase sine reference of 10-A magnitude is applied. The controller response to this abrupt transient is very fast and stable. The slowly damped oscillation that follows is mostly due to modeling errors and, particularly, a bad operation of the grid voltage estimator due to a large parameter mismatch.

2) MPC Based on PWA Model: As shown in Fig. 12, the proposed control scheme is tested using symmetrical triangular PWM to generate the voltage pattern using the same parameters as for the simulation (four different dynamics, horizon $N = 3$, weights are $Q = 100$ and $R = 1$). This time, the small ringing that follows the abrupt transient is damped more quickly. A small distortion can be observed close to the zero crossing; this is due to the low supply voltage (80 V) and to the 1200-V insulated-gate bipolar transistor (IGBT) high conduction losses compared with that of the low voltage. This is partly compensated, together with the interlock time, by the control algorithm.

The controller presents a small static error, which is again amplified due to the reduced voltage level and which will be compensated anyway by the voltage control. It has to be noted that although the controller performance is very good in transient, a control scheme in $d-q$ coordinates will probably perform better in steady state to remove the phase and asymmetry errors. In this case, correction terms should be added to the current-control scheme.

B. Operation as Active Power Filter

1) MPC Based on PWA Model: As shown in Fig. 13, the same control scheme as in Section V-A2 is tested. These results are in accordance with the simulation results presented in Section IV.

2) MPC Based on PWA Model, Observer With Filtered Current, and Capacitor Voltage Measurement: As shown in Fig. 14, the inverter tracks the typical waveform of an active power filter. The filtered current, filtering capacitor voltage, and dc voltages are measured for the control; the inverter current and the grid voltage are estimated using an observer. The steep tracking of the current shows the performance of the hybrid

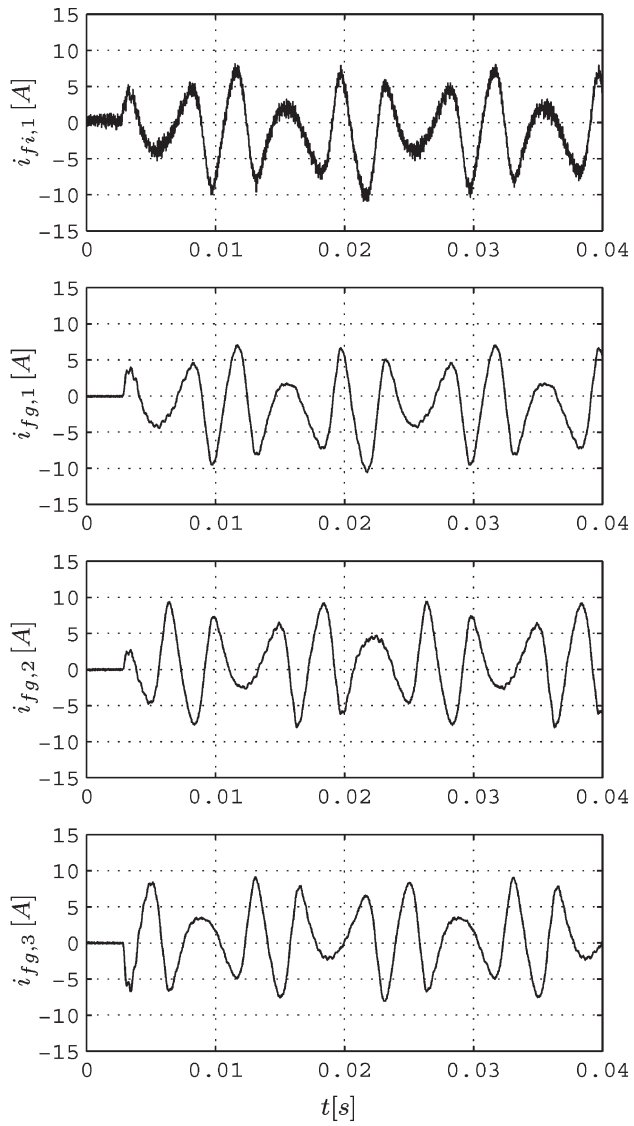

Fig. 13. Experimental plots. MPC with proposed PWA model. (1) Inverter current. (2)–(4) Filtered currents; the three-phase IGBT inverter operates as an active power filter and is filtering the currents of a three-phase diode current rectifier. Ten-kilohertz switching and sampling. Symmetrical triangular PWM modulation. Fifty-hertz grid.

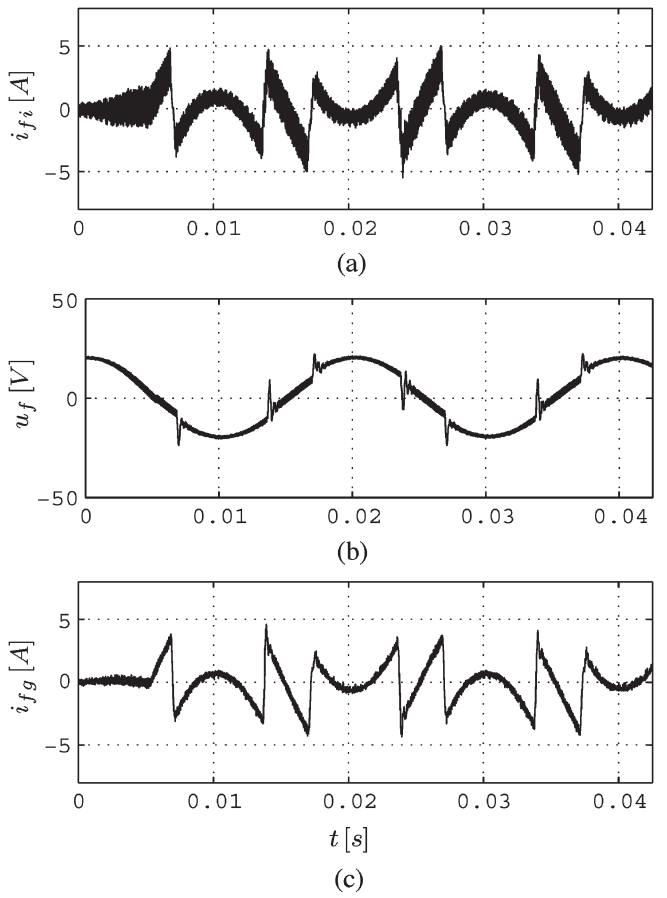

Fig. 14. Experimental plots. MPC with proposed PWA model; the capacitor voltage is also measured for these plots, with the single-phase MOSFET inverter tracking the typical waveform of an active power filter. The steep tracking of the current shows the hybrid MPC controller performance. Ten-kilohertz switching and sampling. Symmetrical triangular PWM modulation. Fifty-hertz grid. (a) Inverter current. (b) Filtering capacitor voltage (V, in seconds). (c) Filtered current.

MPC controller. For these experiments, only a single leg is tested, and there is no nonlinear load connected to the utility grid that is emulated using the two other converter legs that operate at a 100-kHz switching frequency to generate a sine voltage waveform. Compared with the other experiments, there is no ringing in that case, although the transients are more abrupt and the ripple is larger. This is mainly due to the filtering capacitor voltage measurement that considerably reduces the error on the grid voltage estimation and on the observed state. The sensitivity of the control to the system parameters and model increases when the information available diminishes and when the reduction of the estimation errors allows for a better robustness of the controller. The fact that the MOSFET devices present less distortion at low voltage and low current (closer to ideal switches) than the IGBTs might also slightly influence these results.

VI. Conclusion

The classical zero-order old model of the inverter does not capture the switching behavior of the inverter. This might deteriorate the tracking quality or cause stability problems to classical controllers when the filter resonance and switching frequencies are close. This paper has presented two alternative models, both for symmetrical and asymmetrical PWMs, which account accurately for the inverter voltage pattern. An explicit model-predictive controller, which can be based on these PWA models, is derived. The optimal control problem is explicitly solved offline, and the controller is implemented online using a lookup table that has the form of a binary search tree, which allows for a very short execution time. The limitations on the duty cycles are featured as constraints during the design phase, which avoid tuning the weight matrices, thus reducing the design effort.

A state observer and a grid voltage estimator are used to provide the filtered variables to the control and to limit the number of required sensors. The measured variables are the filtered currents and the dc voltage. The grid voltage is estimated quickly and accurately with the proposed scheme. When a very fast dynamic behavior is required, it is, however, crucial to obtain

a good estimation of the grid voltage, insensitive to the system abrupt transients and system parameter mismatches. In this case, the robustness of the system and grid-voltage-estimation accuracy is greatly improved if the filtering capacitor voltages are also measured, resulting in a better dynamic performance and system damping, as shown experimentally.

The proposed control strategy offers very good performance in terms of tracking. It displays a very fast response, and it is very well suited for applications where the current reference is not sinusoidal—e.g., for active filters—or for applications with a weak and distorted grid. The only delay in the response is due to the computation time and PWM response. Future research work will focus on further reducing this delay and improving the grid voltage estimator.

APPENDIX

A. Analytical Derivation of the Model

The autonomous evolution of the system between two sampling instants separated by a time interval T (when both applied grid and inverter voltages are zero) described by the discrete-time equation

$$\boldsymbol{x}(t+T) = \boldsymbol{\Phi}(T)\boldsymbol{x}(t) \tag{21}$$

is obtained by using the following relation:

$$\boldsymbol{\Phi}(T) = e^{\boldsymbol{A}_f \cdot T} \tag{22}$$

with

$$\boldsymbol{A}_f = \begin{bmatrix} 0 & 0 & -\frac{1}{L_{fi}} \\ 0 & 0 & -\frac{1}{L_{fg}} \\ \frac{1}{C_f} & -\frac{1}{C_f} & 0 \end{bmatrix}$$
$$\boldsymbol{B}_f = \begin{bmatrix} L_{fi} \\ 0 \\ 0 \end{bmatrix}$$
$$\boldsymbol{C}_f = \begin{bmatrix} 0 \\ -L_{fg} \\ 0 \end{bmatrix} \tag{23}$$

which yields (24), which is shown at the bottom of the page. With the value of the inductors in parallel L_r, the resonance pulsation ω_r and the system characteristic impedance Z_r

$$L_r = \frac{L_{fi}L_{fg}}{L_{fi}+L_{fg}} \qquad \omega_r = \frac{1}{\sqrt{L_r C_f}} \qquad Z_r = \sqrt{\frac{L_r}{C_f}}.$$

The effect of a pulse of width T and of unity height on the discrete state is described by the following:

$$\boldsymbol{x}(t+T) = \boldsymbol{\Phi}(T)\boldsymbol{x}(t) + \boldsymbol{\Gamma}(T). \tag{25}$$

$\boldsymbol{\Gamma}(T)$ is obtained by integrating

$$\boldsymbol{\Gamma}(T) = \int_0^T e^{\boldsymbol{A}_f \cdot \tau} \cdot d\tau \cdot \boldsymbol{B}_f \tag{26}$$

which yields

$$\boldsymbol{\Gamma}(T) = \begin{bmatrix} -\frac{T}{L_{fg}+L_{fi}} + \frac{L_{fg}}{\omega_r L_{fi}(L_{fg}+L_{fi})} \cdot \sin\omega_r T \\ -\frac{T}{L_{fg}+L_{fi}} - \frac{1}{\omega_r(L_{fg}+L_{fi})} \cdot \sin\omega_r T \\ \frac{1}{\omega_r Z_r L_{fg}} \cdot \cos\omega_r T \end{bmatrix}. \tag{27}$$

B. Symmetrical Modulation Matrices

Using the expressions derived in Appendix A, which gives an autonomous system evolution for an arbitrary time and for an arbitrary pulse, and applying linearity, the evolution of the discrete state with a duty cycle D_0 and a switching time of T_s is obtained

$$\begin{aligned} \boldsymbol{X}_0 = {} & \boldsymbol{\Phi}\left(\frac{2-D_0}{2}T_s\right)\boldsymbol{\Gamma}(D_0T_s)D_0u_{\mathrm{DC}+} \\ & + \left[\boldsymbol{\Phi}\left(\frac{1-D_0}{2}T_s\right) + \boldsymbol{\Phi}\left(\frac{1+D_0}{2}T_s\right)\right] \\ & \times \boldsymbol{\Gamma}\left(\frac{1-D_0}{2}\right)D_0u_{\mathrm{DC}-}. \end{aligned} \tag{28}$$

The approximation of the variation of this evolution for a variation of duty cycles around D_0 is given by the matrix

$$\boldsymbol{B}_p = \left[\boldsymbol{\Phi}\left(\frac{2-D_0}{2}T_s\right) + \boldsymbol{\Phi}\left(\frac{1-D_0-2D_p}{2}T_s\right)\right]\Gamma(D_pT_s). \tag{29}$$

C. Circuit Parameters

IGBT inverter: $L_{fi} = 600\ \mu$H; $L_{fg} = 550\ \mu$H; $C_f = 6.8\ \mu$F; $T_s = 50$; $100\ \mu$s; $f_{\mathrm{res}} = 3.6$ kHz; $u_{\mathrm{nom}} = 750$ V; and $u_{\mathrm{test}} = 80$ V.

MOSFET inverter: $L_{fi} = 330\ \mu$H; $L_{fg} = 300\ \mu$H; $C_f = 3 \cdot 4.7\ \mu$F; $T_s = 100\ \mu$s; $f_{\mathrm{res}} = 3.38$ kHz; $u_{\mathrm{nom}} = 50$ V; and $u_{\mathrm{test}} = 50$ V.

$$\boldsymbol{\Phi}(T) = \begin{bmatrix} \frac{L_r}{L_{fg}} + \frac{L_r}{L_{fi}} \cdot \cos\omega_r T & -\frac{L_r}{L_{fi}} \cdot (1-\cos\omega_r T) & -\frac{1}{\omega_r L_{fi}} \cdot \sin\omega_r T \\ \frac{L_r}{L_{fg}} \cdot (1-\cos\omega_r T) & \frac{L_r}{L_{fi}} + \frac{L_r}{L_{fg}} \cdot \cos\omega_r T & \frac{1}{\omega_r L_{fg}} \cdot \sin\omega_r T \\ Z_r \cdot \sin\omega_r T & -Z_r \cdot \sin\omega_r T & \cos\omega_r T \end{bmatrix} \tag{24}$$

REFERENCES

[1] M. L. Heldwein and J. W. Kolar, "Design of minimum volume EMC input filters for an ultra compact three-phase PWM rectifier," in *Proc. 9th Brazilian Power Electron. Conf.*, 2007.

[2] C. Wessels, J. Dannehl, and F. W. Fuchs, "Active damping of LCL-filter resonance based on virtual resistor for PWM rectifiers—Stability analysis with different filter parameters," in *Proc. IEEE PESC*, 2008, pp. 3532–3538.

[3] S. Mariéthoz, A. G. Beccuti, and M. Morari, "Analysis and optimal current control of a voltage source inverter connected to the grid through an LCL filter," in *Proc. IEEE PESC*, 2008, pp. 3532–3538.

[4] M. Routimo and H. Tuusa, "LCL type supply filter for active power filter—Comparison of an active and a passive method for resonance damping," in *Proc. IEEE PESC*, 2007, pp. 2939–2945.

[5] V. Blasko and V. Kaura, "A novel control of actively damp resonance in input LC filter of a three-phase voltage source converter," *IEEE Trans. Ind. Appl.*, vol. 33, no. 2, pp. 542–550, Mar./Apr. 1997.

[6] M. Liserre, F. Blaabjerg, and S. Hansen, "Design and control of an LCL-filter-based three-phase active rectifier," *IEEE Trans. Ind. Appl.*, vol. 41, no. 5, pp. 1281–1291, Sep./Oct. 2005.

[7] L. A. Serpa, J. W. Kolar, S. Ponnaluri, and P. M. Barbosa, "A modified direct power control strategy allowing the connection of three-phase inverter to the grid through LCL filters," in *Conf. Rec. IEEE IAS Annu. Meeting*, 2005, pp. 565–571.

[8] M. Malinowski, M. P. Kazmierkowski, W. Szczygiel, and S. Bernet, "Simple sensorless active damping solution for three-phase PWM rectifier with LCL filter," in *Proc. IEEE IECON*, 2005, pp. 987–991.

[9] A. Papavasiliou, S. A. Papathanassiou, S. N. Manias, and G. Demetriadis, "Current control of a voltage source inverter connected to the grid via LCL filter," in *Proc. IEEE PESC*, 2007, pp. 2379–2384.

[10] M. Malinowski and S. Bernet, "A simple voltage sensorless active damping scheme for three-phase PWM converters with an LCL filter," *IEEE Trans. Ind. Electron.*, vol. 55, no. 4, pp. 1876–1880, Apr. 2008.

[11] E. J. Bueno, F. Espinosa, F. J. Rodriguez, and S. Cobreces, "Improving perturbation rejection of VSC's connected to the grid through an LCL filter," in *Proc. EPE-PEMC*, 2004. [CD-ROM].

[12] L. Malesani, P. Mattavelli, and S. Buso, "Robust dead-beat current control for PWM rectifiers and active filters," *IEEE Trans. Ind. Appl.*, vol. 36, no. 4, pp. 613–620, May/Jun. 2000.

[13] E. Wu and P. W. Lehn, "Digital current control of a voltage source converter with active damping of LCL resonance," *IEEE Trans. Power Electron.*, vol. 21, no. 5, pp. 1364–1373, Sep. 2006.

[14] J. Rodriguez *et al.*, "Predictive current control of a voltage source inverter," *IEEE Trans. Ind. Electron.*, vol. 54, no. 1, pp. 495–503, Feb. 2007.

[15] G. Papafotiou, T. Geyer, and M. Morari, "Optimal direct torque control of three-phase symmetric induction motors," in *Proc. IEEE Control Decision Conf.*, 2004, pp. 1860–1865.

[16] J. Kley, G. Papafotiou, K. Papadopoulos, P. Bohren, and M. Morari, "Performance evaluation of model predictive direct torque control," in *Proc. IEEE PESC*, 2008, pp. 4737–4744.

[17] G. Papafotiou, T. Geyer, and M. Morari, "Hybrid modelling and optimal control of switch-mode dc–dc converters," in *Proc. IEEE Workshop Comput. Power Electron.*, 2004, pp. 148–155.

[18] L. Corradini, W. Stefanutti, and P. Mattavelli, "Analysis of multi-sampled current control for active filters," in *Conf. Rec. IEEE IAS Annu. Meeting*, 2007, pp. 1608–1615.

[19] A. Bemporad, F. Borrelli, and M. Morari, "Model predictive control based on linear programming—The explicit solution," *IEEE Trans. Autom. Control*, vol. 47, no. 12, pp. 1974–1985, Dec. 2002.

[20] F. Borrelli, *Constrained Optimal Control of Linear and Hybrid Systems*. New York: Springer-Verlag, 2003.

[21] S. Mariéthoz and A. Rufer, "Open loop and closed loop spectral frequency active filtering," *IEEE Trans. Power Electron.*, vol. 17, no. 4, pp. 564–573, Jul. 2002.

[22] J. Löfberg, "YALMIP: A toolbox for modeling and optimization in MATLAB," in *Proc. CACSD Conf.*. Taipei,, Taiwan, 2004, pp. 284–289.

[23] M. Kvasnica, P. Grieder, and M. Baotić, *Multi-Parametric Toolbox (MPT)*, 2004. [Online]. Available: http://control.ee.ethz.ch/~mpt/

Sébastien Mariéthoz (M'05) received the Ph.D. degree in electrical engineering for his work on asymmetrical multilevel converters from the Ecole Polytechnique Fédérale de Lausanne, Lausanne, Switzerland, in 2005.

He was a Research Fellow with the Power Electronics, Machines, and Control Group, University of Nottingham, Nottingham, U.K., focusing on the design and control of new matrix converter topologies. He has been with the Automatic Control Laboratory, Swiss Federal Institute of Technology, Zürich, Switzerland, since 2006, where he is currently a Senior Researcher. His current research interests include power converter topologies, control of power electronic systems with emphasis on model-predictive control, and sensorless control techniques.

Manfred Morari (F'05) received the Diploma degree in chemical engineering from the Swiss Federal Institute of Technology (ETH Zürich), Zürich, Switzerland, and the Ph.D. degree in chemical engineering from the University of Minnesota, Minneapolis.

He was the McCollum–Corcoran Professor of Chemical Engineering and the Executive Officer of the Control and Dynamical Systems, California Institute of Technology, Pasadena. He has been the Head of the Automatic Control Laboratory, ETH Zürich, since 1994. His research interests include hybrid systems and the control of biomedical systems. He has held appointments with Exxon and ICI plc and serves on the technical advisory boards of several major corporations.

Prof. Morari, in recognition of his research contributions, has been the recipient of numerous awards, among them the Donald P. Eckman Award and the John R. Ragazzini Award of the Automatic Control Council; the Allan P. Colburn Award and the Professional Progress Award of the American Institute of Chemical Engineers; the Curtis W. McGraw Research Award of the American Society for Engineering Education; a *Doctor Honoris Causa* from Babeş-Bolyai University, Cluj-Napoca, Romania; Fellow of the International Federation of Automatic Control; and the IEEE Control Systems Field Award. He was elected to the National Academy of Engineering (in the U.S.).